Automatic detection of sand ripple features in sidescan sonar imagery

Anna Crawford
Defence Research & Development Canada,
Atlantic Research Centre
Dartmouth, NS, Canada
Email: anna.crawford@drdc-rddc.gc.ca

Adam Skarke
Department of Geosciences
Mississippi State University
Email: adam.skarke@msstate.edu

***Abstract*—A novel image processing technique, based on fingerprint analysis, is applied to sidescan sonar data in order to automatically extract seabed ripple orientation, wavelength, and defect density parameters. The technique is applied to seabed imagery collected on repeat passes over the same ripple field at headings distributed over 360° in order to evaluate ripple parameter extraction across a range of relative angles between the sonar and dominant ripple orientation. The presence of ripples increases the difficulty of identifying objects of interest in sidescan sonar seabed imagery. The potential for utilizing the density of ripple defects as an objective parameter for the quantification of this difficulty in the context of object detection operations is discussed. Results suggest a number of sidescan sonar data analysis applications that are highly compatible with unsupervised detectors and autonomous mission planning processes.**

I. Introduction

Sand ripples are common features in sedimentary environments and have received increased attention from diverse research communities in recent years. Historically, ripple geometry has been examined as a means of remotely determining qualities of the sediment or whether the forcing mechanism responsible for their formation was reversing (waves) or unidirectional (currents), water or wind driven [1]. Cross-bedded stratification in sedimentary rocks, produced by sand ripples, is used by geologists to determine paleo-environmental conditions [2]. More recently, such techniques have been applied as far afield as Mars [3].

The broad context of the work presented here is seabed mapping for military mine countermeasures (MCM) applications. Within that context, ripples on the seabed can pose a challenge for detection of objects in sidescan sonar survey imagery. The conventional sidescan sonar low grazing angle geometry is designed to allow identification of proud objects in part by the acoustic shadows that are cast. Against a rippled seabed background, the length and width of the shadow are distorted or fragmented as the shadows of the ripple crests combine with those of the object. For Automated Target Recognition (ATR) detection algorithms, first order object features such as size and shape can be obscured [4]. More esoteric features, such as the statistics of the background signal levels, can also be altered. Target detection in the presence of ripples can be problematic even for trained human operators, leading to missed detections and increased false alarm rate.

In MCM operations, an assessment of the "difficulty" of the local seabed for minehunting is a parameter that enters into the survey planning process. There has been little research into how this difficulty is assessed in the case of a rippled seabed, or into objective means of assigning a value. For a rippled seabed, the bulk geometry of the bedform field can be specified in terms of ripple wavelength and orientation, however this does not capture a critical feature of the field, sometimes described as the short- or long-crestedness, the complexity of the ripple field. Some recent work has been done in the characterization of ripples using fingerprint analysis techniques [5]. Among the features used in forensic scientific fingerprint analysis are terminations or bifurcations of print ridges. Sidescan sonar imagery of ripple fields containing defects, the terminations or bifurcations in the ripple crests, is strikingly similar to fingerprint imagery. A larger research goal behind this work is to determine whether ripple defects, or their density, can be useful in parameterizing the difficulty of the seabed for minehunting in the presence of ripples. The work presented here leads toward development of automatic methods for extracting defect density, as well as ripple orientation and wavelength, from sidescan sonar imagery for eventual deployment on autonomous platforms.

Following are descriptions of the fingerprint analysis algorithms (Section II), the test sidescan sonar data set and results of application of those algorithms (Section III) and concluding remarks (Section IV).

II. Automated Ripple Feature Detection Algorithms

There has been considerable previous work in determination of ripple wavelength and orientation in sidescan sonar imagery using filtering or template matching techniques [6]–[8]. The orientation in particular is required for planning of subsequent surveys over rippled areas with the sonar look-angle directed along-crest to mitigate the masking effects of the ripple field in the sonar imagery.

In this work, collected sidescan sonar data were processed with automated routines designed to delineate rippled portions of the sampled domain and calculate the orientation, wavelength, and defect density of the identified bedforms. The

978-1-4799-4918-2/14/$31.00 ©2014 IEEE

employed routines were based on processing algorithms that were initially designed for fingerprint analysis [9]–[11] and subsequently adapted for application to seafloor imagery of rippled bedforms [5].

The initial data processing step normalizes the dynamic range of backscatter intensity across the sidescan sonar image in order to yield a mean of zero and a variance of one. Next a block of pixels, large enough to incorporate multiple ripple wavelengths, is centered on each pixel in the domain and a Gaussian filter is applied to smooth the backscatter intensity values of each pixel within the block. The local ripple crest orientation for each block is defined as the direction orthogonal to the axis of greatest variation in backscatter intensity and assigned to the central pixel of the block. A "reliability" term indicative of the degree to which each block represents a rippled portion of the seafloor is calculated as [1.0 - (backscatter variance parallel to the derived crest orientation / backscatter variance perpendicular to the derived crest orientation)] and this is also assigned to the central pixel of the block. A global threshold is then applied to the reliability values, resulting in a mask that excludes portions of the domain determined not to be rippled from further processing steps.

Ripple wavelength values are determined by dividing the sidescan sonar image into blocks and deriving a profile of backscatter intensity values along a line orthogonal to the mean ripple crest orientation for all pixels in the block. This profile is subsequently smoothed with a Gaussian low-pass filter and ripple spacing is determined by calculation of the median number of pixels between consecutive maxima points in the profile. The window length in pixels used to identify local maxima in the profile is calculated as the number of times the plotted profile crosses its own arithmetic mean, divided by the total length of the profile in pixels. The native resolution of the sidescan sonar image is then used to convert the derived frequency values from pixel units to ripple wavelength values in meters.

To identify the location of ripple defect features, the portions of the domain determined to contain ripples are processed with a two-dimensional Gabor filter, composed of a frequency and orientation selective sinusoidal wave, in order to preserve ripple structure and remove noise. The resulting filtered image is binarized to pixel values of one and zero and the foreground portion of the image (pixel values of one) is iteratively thinned until it is a single pixel wide. In the resulting image, a 3 $\times$ 3 pixel block is centered on each pixel that has a value of one. The central pixel is determined to be the location of a termination defect if the nine-pixel block sum is equal to two and a bifurcation defect if the nine-pixel block sum is equal to four.

The outputs of the complete processing chain are images the same size as the input image containing ripple orientation and wavelength, masked to the area of the image where ripples are found to be present, and a binary image flagging defect locations. Figure 1 illustrates steps in the fingerprint analysis processing from a subsection of an image shown later (Figure 3, on the left).

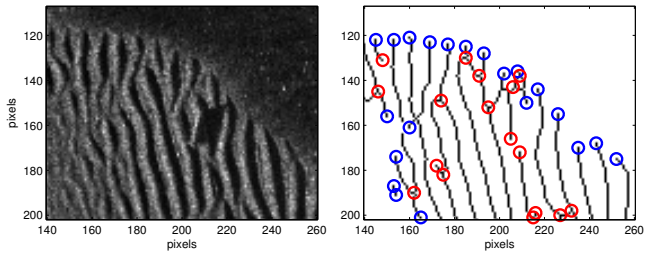

Fig. 1. Example of processing steps in the fingerprint analysis algorithm. (left) Preprocessed sidescan sonar image containing ripples. (right) Thinned binary output from the same image with black lines following ripple crests and bifurcation and termination locations marked by circle symbols. Blue circles indicate termination defects on the edge of the ripple area.

III. Application on a Test Data Set

The test data set that has been chosen for the work presented here was collected in 2008 in Brest Harbour, France, as part of the Canadian Remote Minehunting System (RMS) project during a collaborative trial with Groupe d'Etudes Sous-Marines de l'Atlantique (GESMA). Sidescan sonar data was collected using a Naval minehunting grade sonar, a Klein 5500, deployed on an actively controlled tow body from a semi-submersible autonomous vehicle. This platform provides excellent stability and accuracy in survey line and altitude following. The Klein 5500 operates at 455 kHz, covering a swath 75 m per side with a ground range resolution on the seabed of 20 cm alongtrack by 3 cm acrosstrack. During the trial, multi-aspect survey patterns were run over several inert mine-shaped targets, including a 2.3 m long cylinder. These surveys are designed with a "daisy"-shaped track centred on a target of interest, passing it at fixed range at headings around the compass (see Figure 2), in this case at nominally 15° increments. The outer diameter of the track pattern is around 600 m, with the target falling at approximately 40 m range each time, mid-way across the sonar swath on the same side each pass. The complete survey pattern can be executed by the autonomous vehicle in just over an hour. The original purpose of these surveys was to provide sidescan sonar imagery at a range of headings in aid of ATR research, however, the presence in the target vicinity of a well-formed ripple field is fortuitous for the present work.

The raw sonar data was preprocessed by geo-referencing using the navigation, altitude and attitude inputs from the vehicle and tow body. Positioning accuracy of sidescan sonar imagery in MCM exercises is critical and with the RMS was typically within 3 m of ground truth. The sonar data was gridded on a square East-North grid with 22 cm spacing, slightly larger than the alongtrack ground resolution specification of the sonar to minimize occurrence of inter-ping gaps in the coverage. During the geo-referencing process, the acrosstrack effect of the sonar beam pattern is removed by normalizing the received ping data by an alongtrack-averaged intensity profile. Tiles of normalized geo-referenced sidescan sonar data are produced in 500 ping sections and are output in GeoTIFF and other formats.

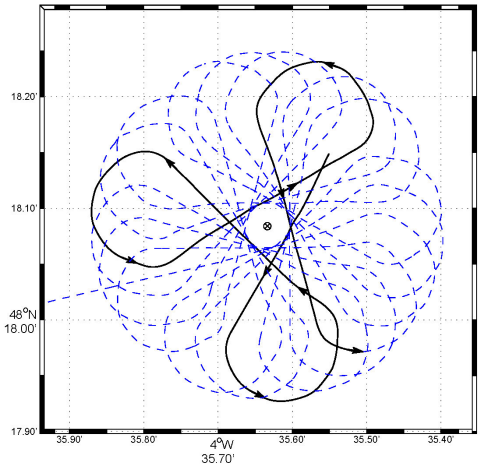

Fig. 2. Multi-aspect sidescan sonar survey track with passes at 15° heading increments centered on a target location. The outer diameter of the track is about 600 m.

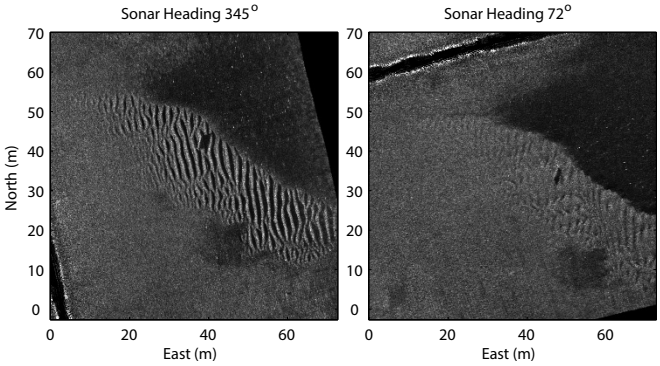

Fig. 3. Samples of geo-referenced sidescan sonar imagery of the same patch of seabed at orthogonal track headings, approximately perpendicular and parallel to the dominant ripple crest orientation. Swath width is 75 m per side.

Examples of geo-referenced sonar data from the multi-aspect survey over the cylinder target are shown in Figure 3 – these have been cropped to the area of interest from larger tiles. The black strip that is the nadir gap directly below the sonar gives an indication of the sonar track heading and location relative to the cylinder which is approximately centred in each image. It is the patch of rippled seabed surrounding the cylinder that is of interest in this work. Due to the side-looking, shallow grazing angle geometry of ensonification, the ripples are well imaged at a sonar heading parallel to the dominant along crest direction, and almost invisible at heading perpendicular to that. This is an effect that can be used to advantage in the planning of follow-up surveys. In addition to the aspect dependence, there are other effects of the imaging geometry. Approaching nadir, the grazing angle goes to normal to the seabed, so the shadow region behind proud objects is reduced to a point below the sonar track where there are no shadows cast. At farthest range, on the outer edges of the swath, acoustic attenuation leads to reduced highlight-shadow contrast in the normalized imagery. The result of these effects is an imaging "sweet spot" for the sonar system, centred around mid-swath, and hence the design of the multi-aspect survey passing the target at about 40 m range.

Samples of the automatic ripple detection output are shown in Figure 4, for sonar track headings of 345° (same as shown in Figure 3 on the left) and 193°. The locations of the bifurcation and termination defects are shown in the leftmost panels of the two series. The terminations along the edges of the ripple areas have been differentiated from those in the interior since these would skew the calculated defect density values. The middle panels show the ripple crest orientation within the area identified as containing ripples, with the colour scale shown on the left. The ripple orientation direction is defined as parallel to the length of the ripple crests using cardinal direction convention (crests aligned North-South have 0° orientation, clockwise is positive from North), i.e. a sonar heading aligned with the ripple crest orientation should provide optimal imaging broadside to the crests. The rightmost panels show the ripple wavelength, also colour-scaled, in meters.

The examples shown in Figure 4 were selected from the set of aspect cases to illustrate particular points about the processing outputs. At 345° heading, the imaging of the ripples was approximately optimal for the orientation. The area defined as containing ripples agrees well with what would be delineated by eye. The second example at 193° heading is between optimal and along crest aspects and shows the steepening grazing angle effect near nadir. A smaller ripple patch has been identified near the top of the image, which shows smaller ripple areas can be determined. At aspects looking approximately along crest (see Figure 3, right side), as expected, the algorithm was not able to determine orientation or wavelength and no rippled area was identified in those images.

A ground truth orientation and wavelength were determined by manually digitizing lines along ripple crests and across from shadow edge to shadow edge at 30 locations distributed around the rippled area in imagery at close to optimal aspect (148° heading). The ground truth mean ripple wavelength was determined as 1.9 m (standard deviation 0.1 m) and orientation 170.5° (standard deviation 2.7°). Interestingly, it proved very difficult to manually determine a comprehensive set of bifurcation and termination locations for the test data set. Comparison between manually identified defects and those located by the automated algorithm showed that obvious defects were correctly identified manually, however the automated algorithm proved to be more consistent and reliable in identifying more subtle defects in the imagery. A ground truth for the defect locations has consequently not yet been determined for this data set and will be the first subject of follow-on research.

Automatically determined ripple features for the complete series of aspects have been compiled, shown in Figure 5. Note that two aspects are missing from the series due to sonar data recording issues. The aspects close enough to along crest that ripple orientation and wavelength could not be determined by

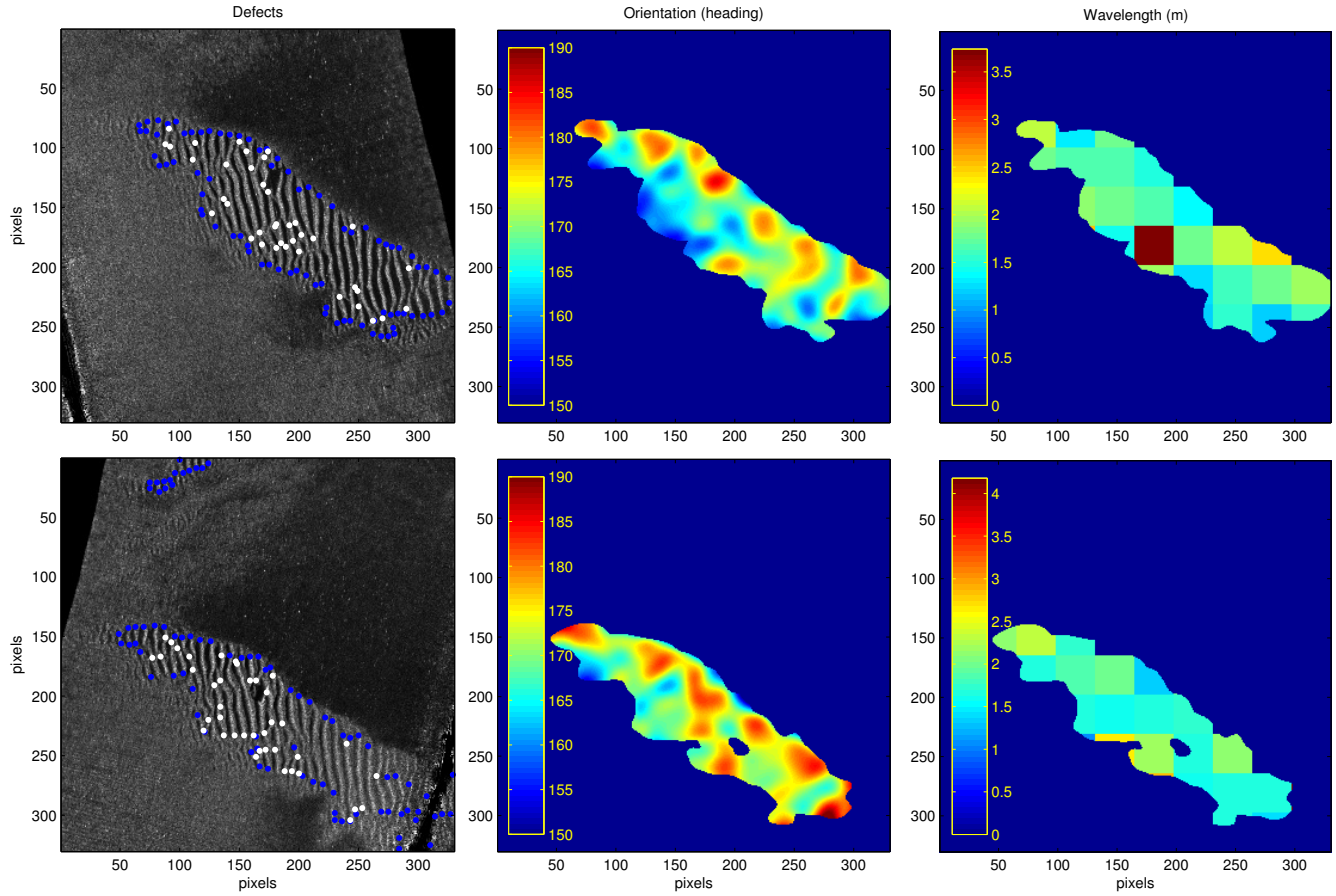

Fig. 4. Samples of processed sidescan sonar imagery at headings 345° in the upper row and 193° in the lower row. (left) Detected defects. Blue dots show terminations on the boundary of ripple areas and white dots show terminations and bifurcations in the interior of the area. (middle) Colour-scaled ripple crest orientation (see text for description of angle convention). (right) Colour-scaled ripple wavelength in meters.

the automated processing are shown with black plus symbols. The ground truth orientation and wavelength are indicated with horizontal lines (plus and minus one standard deviation also indicated). The orientation and wavelength plotted for each aspect are the mean values inside the areas identified as being rippled, like those shown in Figure 4, with error bars sized one standard deviation plus and minus. The defect density is calculated from the number of defects found in the interior of the rippled area, excluding those found on the boundary, divided by the area within the boundary of the defined ripple area.

The best imaging of the rippled area, and subsequently the best results from the automatic ripple feature extraction processing, would be expected at a broadside look-angle to the dominant ripple crest orientation, i.e. at a heading of approximately 170° or 350°. This is confirmed in the summary results shown in Figure 5. The automatically detected wavelength and orientation are consistent with the manually determined ground truth values, with the best agreement near broadside. The standard deviation in orientation and wavelength are also consistent across aspects, and will be in large part due to the natural variability of the ripple field. The 360° coverage of aspect angles gives two approximately equivalent series of results, which agree particularly well in orientation. Using these algorithms, correct determination of orientation is critical for the following steps to determine wavelength and for the ultimate purpose of this work, orientation is an important parameter which could be used to replan a survey at heading perpendicular to the ripples. The range of aspects over which ripple parameters could be determined is wider than the range over which they could not, however a 15° increment is too large to be more specific. Though there is no ground truth for comparison with the defect density results, the automatically determined values are consistent across the range of aspects where a ripple area was defined. The number of located defects drops near the edges of the span of aspect angles over which ripple features can be reliably identified. Visual comparison of automatically determined defect locations between aspects shows identification of obvious defects is consistent, however, further to earlier comments on defect localization, the form of the defects in the imagery has stronger dependence on aspect than the surrounding ripple field. The process of identifying terminations that lie on the boundaries occasionally traps interior defects (an example of that can be seen in Figure 1,

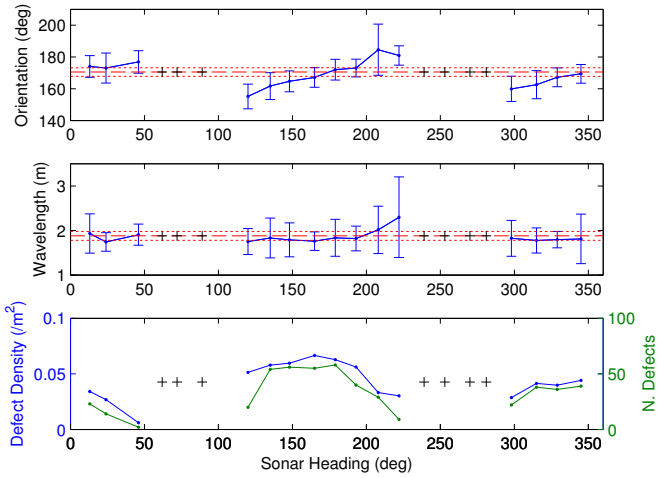

Fig. 5. Summary of ripple mean orientation, mean wavelength and defect density measurements by aspect. "+" symbols indicate headings where orientation and wavelength were not determinable due to an along crest view angle. Error bars on orientation and wavelength are plus/minus one standard deviation. Horizontal lines indicate the ground truth orientation and wavelength values, plus and minus one standard deviation.

along the upper edge of the rippled area), but there will always be pathological cases. The size of the blocks of pixels used in determining the ripple wavelength is evident in the output images on the right in Figure 4. In the upper row of images, comparing the plot of defect locations on the left with the ripple wavelength output, a cluster of defects of approximately the size of a block, located near the center of the image, has affected the local calculated ripple wavelength – examination of the input sidescan sonar imagery shows the algorithm has captured a real feature in the ripple field.

IV. Concluding Remarks

An issue for potential future implementation of the fingerprint analysis algorithms as an automated process is appropriate determination of values for the tunable parameters in the processing. As currently implemented, the algorithms are moderately insensitive to choices in the values for most of the input parameters, e.g. upper and lower bounds on wavelength calculation and width of Gaussian image filters. The sizes of the blocks of pixels that are processed for ripple orientation and then for wavelength can be important – these should scale with the size of the bedform features, so an iterative process may be required for complete autonomy. As mentioned previously, eventual deployment on an autonomous survey platform is a larger goal of this research, and for that application, autonomy is essential.

The occurrence of a suitable ripple field located within the coverage area of a multi-aspect survey is fortuitous. In this case, the ripple crests are long enough that orientation and wavelength are well defined, but there are defects present to be located to test the fingerprint analysis algorithms. At aspect increments of 15°, it is not possible to more specifically define the span of aspect angles over which the automated processing can or cannot successfully determine ripple features in the imagery. The small size of the ripple patch does not lend this data set to more detailed investigation of defect density calculation. The results obtained with this test data set are, however, very promising. Ripple wavelength and orientation were well determined within the range of aspects where the imaging geometry allowed. The work presented here lays the foundation for further investigation into whether defect density can be utilized as a parameter allowing objective and automated description of the complexity, or difficulty, of the ripple field. It is an open research question how this background bedform complexity relates to difficulty of minehunting or to performance of ATR systems.

References

[1] J. R. L. Allen (1993), "Sedimentary structures - Sorby and the last decade", *J. Geol. Soc.*, **150**, pp. 417-425.

[2] D. M. Rubin (1987), *Cross-Bedding, Bedforms, and Paleocurrents*, vol. 1, *Concepts in Sedimentology and Paleontology*, Soc. for Sed. Geology, Tulsa, Okla.

[3] Metz, J. M., et al (2009), "Sulfate-Rich eolian and wet interdune deposits, Erebus Crater, Meridiani Planum, Mars", *J. Sed. Res.*, **79**, pp. 247-264.

[4] Chapple, P. (2008), "Automated Detection and Classification in High-resolution Sonar Imagery for Autonomous Underwater Vehicle Operations", Maritime Operations Division, Defense Science and Technology Organization, DSTO-GD-0537.

[5] Skarke, A. and A. C. Trembanis (2011), "Parameterization of bedform morphology and defect density with fingerprint analysis techniques", *Cont. Shelf Res.*, **31**, pp. 1688-1700.

[6] Maier, I. , and A. Hay (2009), "Occurrence and orientation of anorbital ripples in near-shore sands", *J. Geophys. Res.*, **114**, F04022.

[7] Williams, D., and E. Coiras (2010), "On Sand Ripple Detection in Synthetic Aperture Sonar Imagery", *Proc. 35th IEEE ICASSP*, Dallas, pp. 1074-1077.

[8] Sams, T. , J. Hansen, E. Thisen and B. Stage (2004), "Segmentation of sidescan sonar images", Technical Report of the Danish Defence Research Establishment M-21.

[9] Hong, L., Y. F. Wan, and A. Jain (1998), "Fingerprint image enhancement: Algorithm and performance evaluation", *IEEE Trans. Pattern Anal. Mach. Intell.*, **20**(8), pp. 777-789.

[10] Kovesi, P.D. (2000), *MATLAB and Octave Functions for Computer Vision and Image Processing*, School of Earth and Environment, University of Western Australia.

[11] Thai, R. (2003), *Fingerprint image enhancement and minutiae extraction*, Hons. Thesis, University of Western Australia.